

Physical conditions in the O^{++} zone from ISO¹ and HST data. NGC 6543 revisited.

V. Luridiana and E. Pérez

Instituto de Astrofísica de Andalucía (CSIC), Granada, Spain

M. Cerviño

Instituto de Astrofísica de Andalucía (CSIC), Granada, Spain

Laboratorio de Astrofísica Espacial y Física Fundamental (INTA), Madrid, Spain

ABSTRACT

We revise the physical conditions in the O^{++} zone of the planetary nebula NGC 6543, obtaining two different estimates of the electron temperature (T_e) and one estimate of the electron density (N_e). The electron temperature is computed by means of two independent methods, the nebular-to-auroral ratio $[O\ III]\ \lambda\ 5007/\lambda\ 4363$, and the diagnostic diagram that combines $\lambda\ 5007$ to the $[O\ III]$ infrared lines $52\ \mu$ and $88\ \mu$. The optical and infrared fluxes have been obtained from archive HST/WFPC2 images and ISO LWS spectra respectively, and the continuum intensity in the optical has been measured from narrow-slit spectra obtained with the Isaac Newton Telescope at La Palma. The measured continuum intensity is higher than predicted by recombination theory under the hypothesis that all the $Ly\alpha$ photons either escape or are destroyed. This fact can be explained in terms of an enhancement of the 2-photon continuum due to $Ly-\alpha$ conversion, a process that depends strongly on the local structure of the nebula. Alternative possibilities, outside the framework of recombination theory, have also been considered: e.g., the optical tail in the X-ray emission of a very hot plasma, and dust scattering of stellar radiation, but these hypotheses are not supported by quantitative estimates.

While the electron temperature and density derived from the diagnostic diagram agree with the most recent determination, the temperature derived from $\lambda\ 5007/\lambda\ 4363$, $T_e(O^{++})_{opt}$, is somewhat smaller than previously published values. We discuss several technical issues that contribute to the overall uncertainty in our results, focusing on the instrumental effects that might bias the $[O\ III]\ \lambda\ 4363$ intensity. We also discuss the effects of the collisional de-excitation of the O^{++} ground terms on the relation between $T_e(O^{++})_{opt}$ and $T_e(O^{++})_{IR}$.

Subject headings: instrumentation: miscellaneous—ISM: abundances—planetary nebulae: general—planetary nebulae: individual: NGC 6543

November 3, 2018

1. Introduction

Knowledge of physical conditions (T_e and N_e) is an essential ingredient in the understanding of planetary nebulae. Information on the structure, chemistry and kinematics of these objects comes from individual diagnostics and from the cross-comparison of different diagnostics. In this work, two different diagnostics will be used to investigate the physical conditions in the planetary nebula NGC 6543: the temperature-sensitive [O III] ratio $I(\lambda 5007)/I(\lambda 4363)$, and the (T_e, N_e) diagnostic diagram based on the [O III] optical and infrared lines, which was first proposed by Dinerstein, Lester, & Werner (1985) (henceforth DLW; see also Dinerstein 1983).

The first method, the one based on the $I(\lambda 5007)/I(\lambda 4363)$ ratio, is one of the most popular ones. Advantages of this method are that the lines involved are bright, and close enough to be easily observed with the same instrumental setup; a caution to be taken is that this ratio selectively samples the hottest zones, so that in presence of strong temperature fluctuations the derived temperature, $T_e(\text{O}^{++})_{opt}$, is biased towards the highest values (see, e.g., Peimbert 1995). Furthermore, this ratio measures the temperature of the O^{++} region, which is not necessarily representative of the whole observed volume. The second method, the diagnostic diagram by DLW, allows the simultaneous determination of the electron density and temperature by combining the optical and the FIR fine-structure [O III] lines. The two infrared lines [O III] 52μ and 88μ arise from low-energy levels of the ground term, so their ratio $52\mu/88\mu$ is almost insensitive to the temperature, while the critical densities of their upper levels are different, so the ratio is strongly sensitive to density. On the other hand, a ratio like $\lambda 5007/52\mu$ is strongly dependent on temperature, due to the very different excitation energies of the upper levels of the two lines, and it has a weak dependence on density too, due to the difference in the critical densities. By combining the two line ratios, one can obtain a simultaneous measurement of the electron temperature, $T_e(\text{O}^{++})_{IR}$, and

¹Based on observations with ISO, an ESA project with instrument funded by ESA Member States and with the participation of ISAS and NASA.

density, $N_e(\text{O}^{++})_{IR}$ (we will use throughout the text the subindex *IR* when referring to these T_e and N_e determinations, though an optical line is involved also; this choice responds to simplicity criteria, and highlights the fact that the density is, to a good approximation, a function of the ratio of the two infrared lines alone). One of the main advantages of this method is its internal consistency, since all the lines involved belong to the same ion, so that the same volume is mapped to derive both temperature and density (although the optical and infrared emissivities might follow different distributions within the O^{++} zone if temperature or density fluctuations are present). Two major disadvantages are consequences of the lines involved lying far apart in the spectrum: first, the lines must be observed with different instruments, a procedure implying the risk of systematic offsets in the calibration; and second, any uncertainty in the reddening correction is amplified by the large wavelength baseline.

By means of these methods, we want to reassess the physical conditions in the bright core of NGC 6543. A similar analysis was performed on a small sample of PNe, including NGC 6543 itself, by DLW. These authors used infrared data obtained with the Kuiper Airborne Observatory (KAO), and complemented them with optical spectra from the Lick Observatory Crossley reflector; the analysis was later repeated by Dinerstein, Haas, Erickson, & Werner (1995) (henceforth DHEW), with quite different results. In the work we present here, the intensity of the infrared lines is obtained from ISO archive spectra, and the intensity of $[\text{O III}] \lambda 5007$ and $[\text{O III}] \lambda 4363$ from HST archive images. Additionally, $\text{H}\alpha$ and $\text{H}\beta$ HST images were used to determine the reddening correction to be applied to the other images, and narrow band HST images around $\lambda 6584$ were used to correct the $\text{H}\alpha$ images for the $[\text{N II}]$ contribution. Finally, long-slit, ground-based data obtained with the Isaac Newton Telescope at the Observatorio del Roque de los Muchachos were used to correct the HST images for the contribution of other lines and the continuum. These data will be described in Sections 2, 3 and 4.

1.1. NGC 6543

NGC 6543 (the ‘Cat’s eye’) is a very well known, low-excitation planetary nebula. Many studies have been devoted to understand its complex structure; an incomplete list of the most recent ones includes Reed et al. (1999); Balick, Wilson, & Hajian (2001); Hyung et al. (2001). The bright core of the nebula can be roughly described as the superposition of two ellipses, equal in shape but perpendicular to each other (Miranda & Solf 1992). This region is about $25''$ in diameter, and can be seen in direct images in the Balmer and $[\text{O III}]$ lines. Other structures form part of the nebula: surrounding the bright core, a series of dim concentric

rings is visible in [O III], extending at least out to $70''$ (Balick, Wilson, & Hajian 2001); in turn, the rings are surrounded by a giant filamentary halo of about $300''$ in diameter (Balick, Wilson, & Hajian 2001; Middlemass, Clegg, & Walsh 1989); X-ray emission coming from the bubble surrounding the central star has been recently reported by Chu et al. (2001); the variability of the central star has been investigated by Balick, Wilson, & Hajian (2001).

2. The ISO data

NGC 6543 was routinely observed by ISO for calibration purposes, thereby a large set of spectra is available. We selected 20 out of the 92 Long-Wavelength Spectrometer (LWS) spectra of NGC 6543 available in the ISO data archive, all of them in the AOT L01 observing mode; the selected spectra were taken during two separate periods, close to the beginning and the end of ISO operational life respectively (see Table 1). A detailed explanation of the LWS structure and data sets is provided in *The ISO Handbook, vol. IV, LWS - The Long Wavelength Spectrometer* (Gry et al. 2001).

Each spectrum is comprised of 10 independent wavelength ranges, which correspond to the 10 detectors that form the LWS. These wavelength ranges overlap partially. Both emission lines considered by us fall in the overlap region of two consecutive ranges: i.e., [O III] 52μ falls on both the SW1 and SW2 detectors, while [O III] 88μ falls on both the SW5 and LW1 detectors. Additionally, the spectrum of each of these 10 wavelength ranges is composed of 6 sub-exposures, that correspond to independent scans of the detector. Thus, we can in principle perform, in our sample, $(20 \text{ spectra}) \times (2 \text{ detectors}) \times (6 \text{ scans}) = 240$ independent measures for any of the two emission lines of interest, or 120 with each detector. In practice, the number of independent measurements of a given line with a given detector is smaller than 120, due to the following reasons: in a few cases, one or two out of the six scans of a given exposure do not span the whole detector range, failing to include the line; in other cases the quality of the spectrum is very poor, so that the line-intensity measurement is unfeasible. However, the measurements are still numerous enough (77 on average per line and detector) to adequately sample the data distribution.

The data were reduced using the latest version of the ISO automatic analysis pipeline available in November 2001. The flux measurements were performed by model gaussian fitting. Figure 1 represents the continuum flux versus emission line intensity for all the measurements of the two features, 52μ and 88μ . In the upper plot, the filled dots and the open circles represent the data taken with the SW1 and the SW2 detectors respectively; in the lower plot, the dots and the open circles represent the data taken with the SW5 and the LW1 detectors respectively. The ellipses delimit the region within $1-\sigma$ from the median

values.

Table 2 summarizes the median and dispersion values of the continuum and line measurements for the four detectors. The data of each epoch are shown both as individual data sets, and combined together. The following conclusions can be drawn from the analysis of the data sample:

- a) the SW1 and SW5 continuum data are much more spread out than the corresponding SW2 and LW1 data;
- b) the median intensity values of the 88μ line obtained with SW5 and LW1 are in excellent agreement, whereas the median intensity values of the 52μ line obtained with SW1 and SW2 are more discrepant, although they still agree at the $1\text{-}\sigma$ level;
- c) the median intensity values of the 52μ line obtained with SW1 suffered a drift of more than 1σ from Epoch I (June 1996 + July 1996) to Epoch II (December 1997 + January 1998). This long term drift is known and documented in the ISO LWS Handbook.

Based on these results, we decided to perform our analysis on the line intensities measured with the SW2 and LW1 detectors only, neglecting the data obtained with the other two detectors. The exclusion of SW1 is primarily motivated by the drift in the line flux data, which make them unreliable. On the other hand, the exclusion of SW5 is only motivated by the larger spread in the continuum data with respect to those of the LW1 detector, a feature that does not necessarily imply a lower quality of the line fluxes obtained with this detector. In fact, since SW5 has a spectral resolution twice that of LW1, the recorded dust continuum level per resolution element is lower, making this detector more sensitive to the dark current subtraction: as a result, a fraction of the larger spread in the SW5 continuum data may be caused by the uncertainties in the subtraction of the dark current, an uncertainty not affecting the line fluxes. Nonetheless, we preferred to adopt a conservative approach and exclude both SW1 and SW5 from our analysis. With such a choice, the adopted line intensities are:

$$I(52\mu) = (5.10 \pm 0.61) \times 10^{-10} \text{ erg sec}^{-1} \text{ cm}^{-2} \quad (1)$$

and

$$I(88\mu) = (1.39 \pm 0.17) \times 10^{-10} \text{ erg sec}^{-1} \text{ cm}^{-2}, \quad (2)$$

where the quoted value is the median of the sample, and the uncertainty is the dispersion in the data, which does not include possible systematic error sources, such as, e.g., the flux calibration. These values are in excellent agreement with those reported by Liu et al. (2001),

$I(52\mu) = (5.11 \pm 0.13) \times 10^{-10} \text{ erg sec}^{-1} \text{ cm}^{-2}$ and $I(88\mu) = (1.49 \pm 0.04) \times 10^{-10} \text{ erg sec}^{-1} \text{ cm}^{-2}$, although Liu et al. (2001) quote rather small uncertainties.

A flux correction factor should be applied to take into account the extension of the source, since the ISO LWS analysis pipeline is calibrated on Uranus and it assumes that the target is a point source. This flux correction factor accounts for the relation between the ISO telescope point spread function and the LWS instrumental profile. DLW applied the corresponding flux correction to their KAO data, a correction that was quite small, amounting to only 4% for the 52μ line. In our case, the fraction of flux diffracted out of the aperture is even smaller, and it is therefore negligible with respect to the other uncertainties involved in the process, such as, e.g., the flux calibration itself. Consequently, we did not apply any correction for this effect.

3. The Isaac Newton Telescope long-slit data

NGC 6543 was observed spectroscopically as part of a wider study of PNe on 1995 July 8 and 9. We used the Intermediate Dispersion Spectrograph attached to the 2.5m Isaac Newton Telescope (INT) at the Observatorio del Roque de los Muchachos, on La Palma. The $4' \times 1''$ slit was placed at position angles 5° and 20° , and included the central star. The R1200B grating and the TEK3 CCD in the 235 mm camera provide a dispersion of 0.85 \AA/pixel and a spatial sampling of $0.71''/\text{pixel}$. The seeing was stable at $1.1''$, and the integration time was 1000 s. The spectra were calibrated using the standard steps of flat fielding, bias subtraction, wavelength calibration, and flux calibration using flux spectroscopic standard stars observed during the same night and with the same setup, but through a 10 arcsec wide slit; the spectra were also corrected for light dispersion inside the spectrograph. The inset in the top panel of Figure 2 illustrates the very high quality of these data, showing a logarithmic plot of a sample nebular spectrum in the wavelength range 3400–4500 \AA . These data form part of a much larger data set that will be presented elsewhere.

4. The HST images

The HST data archive at ST-ECF was queried for WFPC2 images of NGC 6543. We retrieved images through the narrow band filters F437N, F487N, F502N, F656N, and F658N, centered on the emission lines $[\text{O III}] \lambda 4363$, $\text{H}\beta$, $[\text{O III}] \lambda 5007$, $\text{H}\alpha$, and $[\text{N II}] \lambda 6584$ respectively. Table 3 summarizes these data sets. For each filter, the different exposures

were combined with the IRAF²/STSDAS command `crrej`, to obtain a final image at each waveband free of cosmic rays. In each of these images, the fluxes were measured within the PC frame of the WFPC2. Similar analyses have been performed by Lane, Harrington, & Borkowski (1997) and Hyung et al. (2001) for NGC 6543, and Rubin et al. (2002) for NGC 7009. Since our results differ from those of both Lane, Harrington, & Borkowski (1997) and Hyung et al. (2001), we will describe our procedure in full detail, so as to allow future identification of the causes behind the discrepancies. The calibration is conceptually straightforward, but the procedure contains several potential pitfalls, such as, e.g., the zeropoint calibration, the adoption of the proper width for the filter, or the estimation of the contribution to the flux of the continuum and of neighbouring lines.

4.1. Photometric zeropoint calibration

The zeropoint of an instrument is defined as the intrinsic flux of an object producing one count per second. The raw data number (DN: the ratio between the electron count in each pixel, and the gain factor, which is 7 in our case) obtained from the HST images must be multiplied by the appropriate zeropoint in order to obtain the flux in energy units. The zeropoint for the WFPC2 is codified in the header word PHOTFLAM. As many other calibration parameters, PHOTFLAM has been periodically modified, as the calibration routine improved. The PHOTFLAM values can be found either in the header of the images, or in the HST-WFPC2 Data Handbook (Baggett et al. 2002). Unfortunately, the two sources give different values; the difference is quite sizeable (almost 4%) in the case of the H α filter F656N, and smaller than 1% for the other filters. As the HST helpdesk advised us to do, we stuck to the PHOTFLAM values of the WFPC2 Data Handbook, which are listed in Table 3.

4.2. Width of the filter

The narrow WFPC2 filters are characterized by several parameters. One of them is the filter’s rectangular width RECTW, defined as the width in Å of a rectangle with the same total area as the total transmission curve, which describes the transmittance of the system, and height given by the peak in the curve. Since the DN is given per unit wavelength, the

²IRAF is distributed by the National Optical Astronomy Observatories, which are operated by the Association of Universities for Research in Astronomy, Inc., under cooperative agreement with the National Science Foundation.

data measured in the WFPC2 images must be multiplied by the RECTW value of the corresponding filter. As already noted by Rubin et al. (2002), RECTW should not be confused with the $\delta\lambda$ values given in the WFPC2 Instrument Handbook (Biretta et al. 2001, Appendix 1). RECTW can be computed for each filter with the IRAF task `synphot/bandpas`. The values for the filters considered in this work are given in Table 3.

4.3. Field of view

The PC frame is a square of 800×800 pixels, corresponding to about $37'' \times 37''$. The central 40×38 pixels were excluded, to avoid contamination by the central star. The outermost pixel rows and columns are affected by optical problems related to the spherical aberration of the telescope. Due to the low photometric quality of these pixel rows they were excluded from our analysis, and the flux was measured in a square of 690×670 pixels, corresponding to about $32'' \times 30''$. This square is smaller than the field of view of the ISO LWS, which has a diameter of about $80''$ at the wavelengths of interest. However, the flux emitted by the nebula is completely dominated by the innermost $30''$, which accounts for more than 97 percent of the total (Figure 3), and the two instruments effectively sample the same area (this is also shown, e.g., by the brightness distribution of the [Ne III] line at 15μ : see Persi et al. 1999). This issue is also addressed by DLW, who match the KAO $40 - 50''$ aperture by taking the ground based observations of [O III] $\lambda 5007$ and $H\beta$ through $45''$ and $70''$ diameter apertures, and using the [O III] $\lambda 4363$ fluxes by Bohuski, Dufour, & Osterbrock (1974) through a similarly wide aperture.

4.4. Flux contribution of neighbouring lines

A fraction of the flux measured in each filter is contributed by lines other than the principal line. In the case of the four filters we considered, F487N and F502N contain only $H\beta$ and $\lambda 5007$ respectively, whereas F437N includes $H\gamma \lambda 4340$ and He I $\lambda 4388$, and F656N includes [N II] $\lambda\lambda 6548, 6584$. In this section, we describe the procedure followed to subtract these contributions from the total measured fluxes.

The total flux of [N II] $\lambda 6584$ was computed from an image taken with the F658N filter, and then subtracted from the F656N image taking into account the transmission efficiency of the filter at the position of $\lambda 6584$. The [N II] $\lambda 6548$ contribution was computed theoretically from the flux of [N II] $\lambda 6584$. Since the F658N filter is, in turn, contaminated by $H\alpha$, the decontamination procedure was iterated to give decontaminated $H\alpha$ and [N II] $\lambda 6584$ flux

values. After this procedure was applied, the total $H\alpha$ flux lowered by about 3%.

The total flux in the F437N filter includes contributions of $H\gamma$ λ 4340 and He I λ 4388. Both contributions are difficult to estimate, since they depend on the exact position of the line in the filter. In the case of He I λ 4388, the intensity of the line itself is also unknown, whereas the total intensity of $H\gamma$ can be computed from $I(H\alpha)$. We estimated these contributions multiplying the nebular spectrum of the long-slit spectra (with the central star excluded) by the F437N transmission curve, and then measuring separately each component on the resulting pattern. The top panel in Figure 2 shows the nebular spectrum of NGC 6543 along position angle 5° in the wavelength region around $H\gamma$ 4340, [O III] 4363 and He I 4388. The dashed line is the actual spectrum, while the full line is this spectrum convolved with the HST F437N filter response (the total system peak response of 0.03 (Biretta et al. 2001) has been divided out so as to make the two spectra comparable). The inset shows a sample of the spectrum along the slit in a logarithmic scale, to provide an indication of the high S/N of this data set. We found that $H\gamma$ and He I λ 4388 contribute on average 12% and 4% respectively to the total flux in F437N, while [O III] λ 4363 provides on average 26% of the flux, with a typical deviation of 3%. This is plotted in the bottom panel of Figure 2, which shows the contribution of λ 4363 to the total intensity in F437N, normalized to 100 (dotted circles, left handside scale; the central $\pm 3''$ are excluded from the analysis); the rest of the flux detected through the filter is contributed by $H\gamma$ and He I 4388, other very faint emission lines, and by the underlying nebular continuum (see top panel). Also plotted for reference is the variation of the [O III] 4363 line intensity along the slit (solid line, right hand side scale).

4.5. Continuum subtraction

The underlying continuum contributing within each of the HST images can be ascertained either theoretically or empirically. The first method requires a detailed computation of the efficiency of all the processes involved, while the second consists in measuring on a spectrum the relative importance of each line with respect to the underlying continuum, with the filter’s transmittance curve taken into account. We chose to do it both ways, since the comparison between the results illustrates quantitatively the difficulties of an accurate theoretical computation of the nebular processes.

4.5.1. Theoretical continuum contribution

The processes contributing to the nebular continuum flux are H I, He I, and He II recombination, bremsstrahlung, and 2-photon decay. The relative importance of these processes depends on both the wavelength and the nebular electron temperature, and on the He I and He II abundances. Table 4 shows the frequency dependence of the continuum-emission coefficient, γ_ν , for each process at the three wavelengths of interest, in units 10^{-40} erg cm³ sec⁻¹ Hz⁻¹; the data have been obtained interpolating in the $(\nu, \log \gamma_\nu)$ plane between the values listed by Brown & Mathews (1970) at $T_e = 8000$ K.

The 2-photon continuum intensity is quite difficult to compute accurately, as it depends not only on the local physical conditions N_e and T_e , but also on the fate of the Ly α photons produced by recombination. In optically thin or dusty nebulae, all the electrons on the 2²P level produce a Ly α photon that eventually escapes from the nebula or is destroyed by dust, whereas those on the 2²S level decay to the ground state producing 2-photon continuum, the population on 2²S and 2²P levels being determined by the recombination cascade and the mutual collisional transitions. In practice, Ly α photons can be scattered repeatedly before they escape from the nebula, and at each scattering the absorbing electron has a finite probability of suffering a 2²P \rightarrow 2²S transition and decaying via 2-photon emission. Thus, with given local physical conditions (N_e, T_e) , the actual 2-photon emission can vary from a minimum value (corresponding to the case in which all the Ly α photons are either destroyed by dust or escape from the nebula) to a maximum value (corresponding to the case in which all the Ly α photons are eventually converted to 2-photon continuum). In Table 4 and Figure 4 we represent, as a function of the wavelength, the two limiting values for the 2-photon continuum, and the corresponding values for the total continuum. The impact of the occurrence of Ly α conversion on the total continuum level depends on the wavelength considered; in the case of the wavelength range around λ 4363, where 2-photon emission is a dominant process, Ly α conversion can enhance the total continuum by as much as a factor 2.5. This would be the asymptotic case of a very thick, dust-free nebula, and represents just an upper limit to be considered in the following. We assumed in the calculations $T_e = 8000$ K and $N_e = 1650$ cm⁻³; the density corresponds to the observed 52 μ /88 μ ratio: see Section 5. The collisional rates listed by Osterbrock (1989) for the 2²S \rightarrow 2²P transition have been linearly extrapolated in temperature down to $T_e = 8000$ K; this might seem a rough approximation, but our results are fairly insensitive to it, both because the collisional data at $T_e = 10000$ and 20000 K are quite similar, and because collisions are outnumbered by spontaneous decays at these nebular conditions anyway.

The He II recombination continuum is not listed because it is not relevant for NGC 6543, due to the low He⁺⁺ abundance $(N(\text{He}^{++})/N(\text{H}^+) \sim 10^{-4})$, Hyung et al. 2000). On

the other hand, $N(\text{He}^+)/N(\text{H}^+) \sim 0.11$, so that the He I recombination continuum cannot be neglected.

The continuum-emission coefficient j_ν , measured in $\text{erg sec}^{-1} \text{ cm}^{-3} \text{ Hz}^{-1} \text{ ster}^{-1}$, is related to γ_ν through $j_\nu = N_+ N_e \gamma_\nu / 4\pi$. Figure 4 shows j_ν normalized to $N(\text{H}^+) N_e / 4\pi$, i.e., the He I recombination contribution has been multiplied by the factor $N(\text{H}^+)/N(\text{He}^+)$, so that the contributions of the three processes to the continuum can be directly compared. The specific intensity emitted through each process depends on the width of the filter’s passband RECTW: $I_\nu = \int_{\text{RECTW}} j_\nu d\nu = N_+ N_e / 4\pi \int_{\text{RECTW}} \gamma_\nu d\nu$.

The continuum contribution is very important in filters centered on weak lines, such as [O III] $\lambda 4363$, but it barely affects the intensity in filters centered on strong lines, such as H α or [O III] $\lambda 5007$. Our computations show that, at $T_e = 8000$ K and neglecting Ly α conversion, the continuum yields 40% of the total intensity in the F437N filter around [O III] $\lambda 4363$, 0.3% of the total intensity in the F502N filter around [O III] $\lambda 5007$, and 0.5% of the total intensity in the F656N filter centered on H α . As anticipated before, we also measured the continuum contribution on long-slit spectra, and compared it to our theoretical computations. Our findings are discussed in next section.

4.5.2. Continuum contribution from direct measurement

The expected continuum intensity can be compared to direct measurements of the continuum level in an optical spectrum. We followed this procedure measuring (through the corresponding filter responses, as described in section 4.4) the integrated continuum flux and relevant line intensities in the two long-slit spectra of NGC 6543 described in Section 3. By means of this procedure, we find that the continuum contributes 58% of the total intensity in the F437N filter around [O III] $\lambda 4363$ (cf. Figure 2), significantly more than expected on the basis of our previous calculations.

Three likely candidate mechanisms that would enhance the continuum level are X-ray emission, dust scattering, and 2-photon emission. X-ray diffuse emission has been recently reported from high resolution spectral images by Chandra (Chu et al. 2001); this is produced in the mass-loading shocked region where the fast stellar wind interacts with the inner gaseous shell. The optical tail of such emission could be the origin of the observed extra continuum. To test this point, we modeled the central cavity of NGC 6543 by means of simple, spherical hot-plasma models at different temperatures, normalized to the soft X-ray flux observed by Chandra, and computed for each model the contribution to the F437N band. Large uncertainties in this calculation are introduced by the values assumed for the

plasma temperature, the exact lower energy limit seen by Chandra (which is around 0.1 – 0.2 keV), and the intervening absorption by neutral gas (which we did not take into account in our estimates). For example, a $T = 1.7 \times 10^6$ K plasma, normalized to the emission in the (0.1 – 10 keV) interval, produces only 0.001% of the observed extra-continuum in F437N, while a $T = 5 \times 10^5$ K plasma, normalized to the emission in the (0.4 – 10 keV) interval, produces 10% of the observed extra-continuum in F437N. Although these are only back-of-the-envelope computations, altogether they suggest that the extra continuum cannot be explained in terms of hot plasma emission.

A different mechanism that could explain the extra continuum is dust scattering of the central star’s radiation. Even if the external screen extinction is rather small, $C(\text{H}\beta) = 0.07$ (see below), a cursory inspection of SWS+LWS archival spectra of NGC 6543 shows a thermal bump due to hot dust peaking at $\sim 30\mu$. Although this mechanism is a plausible candidate for the origin of the extra continuum, the detailed modeling of the internal dust distribution in NGC 6543 is beyond the scope of this paper.

A third possibility is 2-photon emission with enhanced efficiency. As discussed in Section 4.5.1, in our estimate of the 2-photon emissivity we made use of a simplified treatment (Osterbrock 1989; Brown & Mathews 1970), which neglects $\text{Ly}\alpha$ conversion. The efficiency of $\text{Ly}\alpha$ conversion to produce 2-photon emission varies between 0 in optically thin or dusty nebulae (all the $\text{Ly}\alpha$ photons either escape or are destroyed by dust) and a maximum (all the $\text{Ly}\alpha$ photons are eventually converted to 2-photon emission). The detailed calculation of the actual efficiency of this process is virtually impossible, since it would require knowledge of the local escape probabilities and the dust structure of the nebula, and the implementation of this information in a 3-D computation. The only feasible alternative is to bracket this process by computing the 2-photon emission in the extreme case of maximum efficiency. Following the formalism of Brown & Mathews (1970), it is found that the 2-photon emission at $\lambda 4363$ can be enhanced by $\text{Ly}\alpha$ destruction by up to a factor of 3.5, rising the total continuum by up to a factor of 2.5. Figure 5 compares the observational data to the continuum range predicted by recombination theory, as a function of the $\text{H}\gamma$ intensity. The data are compatible with a $\text{Ly}\alpha$ -conversion enhancement of the 2-photon continuum, and suggests that it is not necessary to invoke other processes to explain the measured continuum level (the only discrepant points are some of those with the lowest intensity values, i.e. with the largest errors). The figure also shows that the relation between $\text{H}\gamma$ and the measured continuum is not linear, and that there are large fluctuations around the best-fit straight line, as expected if the continuum in excess of the minimum level arises from $\text{Ly}\alpha$ conversion: stated otherwise, the $\text{Ly}\alpha$ conversion process acts with different efficiency across the nebula. This figure demonstrates that it is not possible to rely on theoretical calculations alone to correct the total flux in each image for the continuum contribution: first because we would

ignore, a priori, the average efficiency of the Ly α conversion process (the slope on the H γ -continuum relation, which is provided by the slit spectrum); second because, even with this piece of information available, we would still ignore the large fluctuations of the continuum around such average level. These fluctuations naturally arise as a consequence of the local character of the 2-photon enhancement process, and, since theory alone provides no way of predicting where and how large they are across the image, they would translate directly into an uncertainty in the measured λ 4363 flux. Furthermore, this uncertainty would be relatively much larger for λ 4363 than it is for the continuum, since the relative contribution of the line in the F437N filter is less than one half that of the continuum, so that a typical uncertainty of, e.g., 20% in the continuum would translate into an uncertainty of 45% in the line. This would be much larger than the typical uncertainty that can be read directly from Figure 2, and it would not avoid the need for a spectroscopic measurement; so this strategy to determine $I(\lambda$ 4363) across the image is definitely not viable.

Note also that this conclusion holds even under the hypothesis in which the 2-photon continuum is at its minimum level (the only case that would allow to predict the continuum produced by recombination by means of a recombination line) and that the additional continuum flux comes instead from a different source: as a matter of fact, the continuum is not proportional to H γ , hence it cannot be predicted theoretically, no matter which process is responsible for the departure from direct proportionality. An important consequence is that no temperature maps can be obtained using this kind of data, unless very specific circumstances occur: one would be that λ 4363 dominate the light in the filter, so that only a rough correction for the continuum would suffice; a second one would be the availability of tunable filters to measure directly the continuum level near λ 4363, bypassing the need for theoretical predictions. The lesson to be learned from these computations is that precision photometry of weak lines cannot be done with the HST/WFPC2 in the absence of data specifically designed to measure the continuum. As a matter of fact, an additional uncertainty is introduced even by the estimation of the contribution of the various lines inside each filter, unless a reliable calibration is available. Both these problems and possible solutions to them - continuum and line subtraction - have been addressed by O’Dell & Doi (1999) and O’Dell, Peimbert, and Peimbert (2003); their arguments will be described in Section 6.1. To proceed with the discussion, we will therefore assume that the λ 4363 percentage within the filter F437N is the one provided by the bottom panel of Figure 2, i.e. $I(\lambda$ 4363)/ $I_{tot}(\text{F437N}) = 0.26 \pm 0.03$. It must be emphasized, however, that in the absence of slit spectra or sophisticated theoretical tools to estimate a priori the continuum intensity, such uncertainty would be much larger, amounting to the difference between the minimum and maximum continuum value admitted by recombination theory.

In their paper on NGC 6543, Hyung et al. (2001) pointed out inconsistencies between

the theoretical estimation and the continuum level derived from observations (in their case, ground-based echelle spectra). It is not clear, however, whether such inconsistencies can be tracked down to what we point out in this work, as their procedure differs from ours in at least two relevant aspects: first, the theoretical continuum flux computed by Hyung et al. (2001) includes only the contributions by H I recombination and bremsstrahlung. However, Fig. 1 in Brown & Mathews (1970) shows that, at $T_e = 10000$ K, the continuum is dominated by 2-photon continuum at $\lambda 4363$, and this process is only slightly less important than H I recombination at $\lambda 5007$. At $T_e = 8000$ K the 2-photon contribution is even more important. The 2-photon continuum must therefore be included even in a rough estimation of the theoretical continuum flux. Second, Hyung et al. (2001) adopt smaller values than we did for the width of the filter: 25.2 Å, 26.9 Å, and 21.9 Å for F437N, F502N, and F656N respectively, instead of 31.829 Å, 35.781 Å, and 28.336 Å. Apparently, these values correspond to the effective width of the bandpass $\delta\lambda$ defined by Biretta et al. (2001) (pag. 149 and Appendix 1; see also Section 4.2 above); however, we might be misunderstanding their procedure, since this point is not explicitly stated in their paper, and their H α width slightly differs from the one given by Biretta et al. (2001). But if we are understanding their procedure, then the difference in the adopted filter widths propagates directly into differences in the estimated continuum flux. This introduces a large bias in all the derived fluxes. Furthermore, since the ratios of different RECTW values are not equal to the ratios of different $\delta\lambda$ s, the intensity ratios of different images are correspondingly affected (the way it affects the derived $\lambda 4363$ is more subtle, because the continuum contribution to be subtracted from the F437N flux is directly proportional to the adopted bandwidth).

It seems probable that Lame, Harrington, & Borkowski (1997) also relied on a theoretical computation to estimate the theoretical continuum in the F437N image, since the number they quote, $F_c(\text{F437N}) = 0.015 \times F(\text{H}\beta)$, is comparable (actually, smaller) than our theoretical computation. However, their work is just a short conference contribution, and they do not specify how such estimate is obtained.

A similar procedure was also followed by Rubin et al. (2002) in their analysis of the planetary nebula NGC 7009. These authors obtain a temperature map of NGC 7009 by means of WFPC2 images taken in the same filters considered by us. To estimate the line contribution inside the WFPC2 filters, they make use of HST/STIS data, modified to take into account the transmittance of the corresponding WFPC2 filters. Following this procedure, they find that the continua measured from STIS are higher than expected at the temperature of the nebula. They interpret such discrepancies as an artefact due to insufficient signal-to-noise in the STIS data, and therefore adopt in their analysis a continuum flux from theoretical computations; it is possible, however, that the problem they found with the continuum in NGC 7009 is analogous to what is found in NGC 6543, namely 2-photon continuum enhancement.

In any case, the uncertainty on the continuum is less crucial in their work than it is in the case of NGC 6543, because $\lambda 4363$ is relatively more intense in NGC 7009: they measure in F437N a $\lambda 4363$ /continuum ratio equal to 3.7, i.e. almost one order of magnitude higher than the one observed in NGC 6543.

Summarizing this section on continuum, it is important to stress that there is no safe way to predict accurately the $\lambda 4363$ contribution to the total flux in the filter F437N, unless this line is very bright. Because of this difficulty, special care should be given to this point, and the relevant assumptions should always be made explicit.

4.6. Reddening correction

The mean value of the $H\alpha/H\beta$ flux ratio across the HST image of NGC 6543, with the [N II] and the continuum contributions subtracted, is $H\alpha/H\beta=3.06\pm0.12$ (cf. Figure 6). Adopting the extinction law by Cardelli, Clayton, & Mathis (1989) with $R_V=3.0$, and fitting to the theoretical Balmer decrement at $T_e = 8000$ K (Storey & Hummer 1995), a reddening coefficient $C(H\beta) = 0.07 \pm 0.06$ is obtained.

The three $C(H\beta)$ values compiled by Hyung et al. (2001), $C(H\beta)=0.18, 0.20$ and 0.30 , are significantly higher than our result. We ignore the origin of this discrepancy, since none of the papers referenced by Hyung et al. (2001) lists the observed $H\alpha$ fluxes, nor do they provide details on the assumptions underlying the computation of $C(H\beta)$. On the other hand, our adopted $C(H\beta)$ agrees with the value determined by other authors. For example, Kaler (1983) found $C(H\beta)=0.10$, and the average value from the literature compilation by Kaler, Shaw, & Browning (1997) is $\langle C(H\beta) \rangle = 0.09$.

5. Density and temperature in the O^{++} zone

The line intensities obtained by the measured fluxes after dereddening and empirically correcting for continuum contribution, are:

$$I(\lambda 4363) = (3.95 \pm 0.84) \times 10^{-12} \text{ erg sec}^{-1} \text{ cm}^{-2}, \quad (3)$$

and

$$I(\lambda 5007) = (1.93 \pm 0.29) \times 10^{-9} \text{ erg sec}^{-1} \text{ cm}^{-2}, \quad (4)$$

The quoted uncertainties have been estimated as follows: the uncertainty on $C(\text{H}\beta)$, 0.06 dex, translates into uncertainties of 0.07 dex and 0.06 dex for $\lambda 4363$ and $\lambda 5007$ respectively; the continuum subtraction adds another 0.05 dex to the uncertainty on $I(\lambda 4363)$ (Section 4.5.2); finally, further uncertainties should be added to account for the shift in wavelength of the bandpass with temperature, and the photometric errors (cf. Biretta et al. 2001, Table 8.11); however, this is a very complex issue, as it will be shown in Section 6.1.1, and this source of uncertainty will not be considered for the moment.

These values yield $\lambda 5007/\lambda 4363 = 490 \pm 130$, and $T_e(\text{O}^{++})_{opt} = 7500 \pm 450$ K, a temperature lower than previously published values. For example, Hyung et al. (2001) find $T_e = 8000 \sim 8300$ K, Kingsburgh, López, & Peimbert (1996) find $T_e = 7950 \pm 100$ K, Peimbert, Torres-Peimbert, & Luridiana (1995) find $T_e = 8334$ K, and DLW adopt $\lambda 5007/\lambda 4363 = 363$ from Bohuski, Dufour, & Osterbrock (1974), which yields, using the same atomic data as us, $T_e(\text{O}^{++})_{opt} = 7900$ K.

Combining the infrared intensities measured on ISO spectra with the $[\text{O III}] \lambda 5007$ intensity derived from the HST data, it is possible to simultaneously derive the temperature and density in the O^{++} zone of NGC 6543 by means of the infrared-line diagnostic described by DLW. The diagnostic diagram is shown in Figure 7, where the point representing the data has been plotted. The data points by DLW and DHEW are also plotted. The values obtained are $N_e = 1650^{+550}_{-400} \text{ cm}^{-3}$, $T_e = 8600 \pm 500$ K, while the corresponding values quoted by DLW and DHEW are $N_e = 10000^{+\infty}_{-6000} \text{ cm}^{-3}$, $T_e = 5800 \pm 300$ K and $N_e = 2000^{+500}_{-400} \text{ cm}^{-3}$, $T_e = 8500 \pm 500$ K respectively.

Figure 7 and Table 5 show that the point by DLW and the one we obtain here disagree by much more than 1σ , both in T_e and N_e . The three lines are discrepant, particularly 52μ and $\lambda 5007$ (however, the discrepancy in $\lambda 5007$ depends solely on the adopted $C(\text{H}\beta)$, since the difference between the measured fluxes is less than 1%). These differences go in the same sense, so that the $\lambda 5007/52\mu$ ratio is not very different in the two cases: however, the upward bending of the isotherm contours in the high-density region of the diagram enhances the difference between the corresponding temperatures. On the other hand, our results are in excellent agreement with those by DHEW, though unfortunately the fluxes of individual lines cannot be compared since they were not published.

5.1. The comparison between $T_e(\text{O}^{++})_{opt}$ and $T_e(\text{O}^{++})_{IR}$

In the presence of temperature variations across a low-density, homogeneous nebula, it is well known that $T_e(\text{O}^{++})_{opt}$ preferentially weighs regions of high T_e , while $T_e(\text{O}^{++})_{IR}$

preferentially weighs regions of lower T_e . In such a case $T_e(\text{O}^{++})_{opt} \geq T_e(\text{O}^{++})_{IR}$, with the equality holding in the constant-temperature case. When density fluctuations are also present, this basic scenario complicates, because the temperature is lower in the densest zones, and because collisional de-excitations of the infrared lines may play a role. Roughly, we expect higher $T_e(\text{O}^{++})_{IR}$ values due to the collisional suppression of the $52\ \mu$ line; as a result, $[T_e(\text{O}^{++})_{opt} - T_e(\text{O}^{++})_{IR}]$ may become negative. Since density fluctuations are certainly present in the nebula, as revealed by the filaments and thin shells seen in the $\text{H}\alpha$ images of the nebula, the value we determined for $T_e(\text{O}^{++})_{IR}$ is totally plausible.

Summing up, our $T_e(\text{O}^{++})_{opt}$ does only marginally agree with the published values; $T_e(\text{O}^{++})_{IR}$ agrees with the most recent of the only two determinations we know of; and $T_e(\text{O}^{++})_{IR}$ compares well with the expected value of $T_e(\text{O}^{++})_{opt}$ (higher than ours by $\sim 400 - 800$ K), provided there are high density zones in the nebula, which depress the flux in $52\ \mu$. In the following, we will list and discuss the uncertainties affecting our results. In this discussion we will consider several uncertainties affecting all the data, although, in the light of the preceding discussion and the previous comparison to published data (see Section 5), it seems probable that the problem lies with the adopted WFPC2 $\lambda 4363$ flux, and that our ISO infrared data and the WFPC2 $\lambda 5007$ data are reasonably accurate.

6. Possible sources of error

6.1. Continuum subtraction in F437N

The long slit on which the continuum level was measured samples only one fraction of the whole nebula, and we cannot guarantee that such fraction is indeed representative of the rest. It seems not probable, however, that the continuum varies so dramatically in the area outside the slit, so as to alter sensibly our conclusion. A further possibility is a bias in the continuum level of the slit spectra. A bias in the continuum level could be caused by at least two different circumstances: an inaccurate correction for light dispersion inside the spectrograph, and scattered light from the central star within the nebula. The first effect could be important in view of the fact that the flux in the continuum outweighs the flux in $\lambda 4363$ in the filter, so that a small bias in the continuum would be amplified in the derived $\lambda 4363$ value. The second effect, which would mimic a more intense nebular continuum, would affect equally the slit spectra and the HST images, so it cannot be invoked as a cause for the low $T_e(\text{O}^{++})_{opt}$ found, and will not be further discussed.

O'Dell & Doi (1999) stress the importance of an accurate calibration of the WFPC2 filters in order to make a quantitative use of the HST emission-line images. One of the

problems they discuss related to calibration is that the filter characteristics described in the WFPC2 Handbook have been determined in parallel light, whereas the incident beam inside the WFPC2 is convergent. The consequence is that the filters *as used by the WFPC2* have shorter peak transmissions and wider FWHMs. The use of the pre-launch filters’ characteristics provided with the HST documentation can therefore introduce a bias, and they recommend instead the use of calibration relations based on the instrument “as used”. A specific problem they address is the continuum subtraction; the strategy they suggest to determine the continuum level is to use an image taken in F547M, a filter that includes no prominent emission lines, together with an assumption on the color of the continuum. Unfortunately, NGC 6543 has not been observed in this filter, so this method is not applicable in our case.

A different strategy to subtract the continuum from the F437N filter has been proposed by O’Dell, Peimbert, and Peimbert (2003) for the case of low-excitation objects. The basic idea is to take an image in the F469N filter: the constraint on the excitation degree of the object ensures that the contribution of the He II line $\lambda 4686$ is negligible, and all the signal in the image can be interpreted in terms of continuum. This procedure allows to reduce the uncertainty related to the assumption on the color of the continuum, since the distance between the wavelengths of F437N and F469N is quite small. Unfortunately, although the $\text{He}^{++}/\text{H}^+$ ratio in NGC 6543 is very small and make this object suitable to apply the method by O’Dell, Peimbert, and Peimbert (2003), no F469N image of this object has been obtained (maybe it is precisely *because* the $\text{He}^{++}/\text{H}^+$ ratio in NGC 6543 is so small, that an observation of the nebula with this filter was judged uninteresting by past observers).

6.1.1. Other issues related to the HST/WFPC2 calibration

There are further possible explanations for our anomalous $T_e(\text{O}^{++})_{opt}$ result related to the WFPC2 calibration. We will give a broad overview of them, without estimating them quantitatively.

One problem is the accuracy in the determination of the contribution of the various lines in each filter. Due to the nature of the calibration procedure mentioned in the previous section, together with the natural changes suffered by any filter with time, the specifications reported in the WFPC2 Handbook do not necessarily give an accurate description of the actual filters’ transmission curves. As a result, the decontamination of the F656N flux from the $[\text{N II}] \lambda 6584$ contribution could be slightly biased; and the decontamination of the F437N flux from the $\text{H}\gamma$ contribution could be even more biased. Unfortunately, the relations provided by O’Dell & Doi (1999) to deal with this problem are not applicable, because they

make use of the flux in the F547M filter, which has not been used to observe NGC 6543.

There are also other potential problems that affect only faint images with very low DNs. The composite F437N image used in the study has a mean DN of 2.9, corresponding on average to $\text{DN} \sim 1.5$ in each of the two exposures (the DN cannot be measured individually on these two images, since it is spuriously increased by cosmic rays, which are removed in the composite image); since these DNs are extremely low, the effects mentioned in the following are possibly a large source of uncertainty in the F437N flux. On the other hand, the images taken with the other filters have DNs of the order of hundreds, and their calibration is much more accurate.

Further relevant sources of uncertainty, which affect all CCDs at low DNs, are the read noise and the loss of information implied by the digitization of the signal. Another important source of uncertainty in our specific case is the progressive alteration in the performance of the WFPC2 CCDs: in orbit, the CCDs are subject to radiation damage (Biretta et al. 2001), which alters their long term properties leading to an increase in dark counts and a decrease in the charge transfer efficiency (CTE). Dark counts increase because of hot pixels, which are routinely identified and can, in principle, be corrected. Conversely, the decrease in CTE is difficult to estimate, since the existing calibrations (Whitmore, Heyer, & Casertano 1999) are based on measurements of the CTE loss for a bright point source ($\text{DN} \gtrsim 60$ for gain = 7) observed against a faint background ($\text{DN}_{bg} \lesssim 1$ for gain = 7); therefore, it is not clear whether the correction formulae provided by Whitmore, Heyer, & Casertano (1999) can be equally applied to the case of a diffuse, nebular object, which can be seen as a moderately faint object seen against a moderately faint background (in our case, $\text{DN} = \text{DN}_{bg} \sim 1.5$ for gain = 7). On the other hand, Figure 4.14 in Biretta et al. (2001), based on recent observations, includes a few more points for brighter backgrounds, in addition to those on which the calibration by Whitmore, Heyer, & Casertano (1999) was based. The behavior of the recently added points suggests that the CTE does not depend on the DN for backgrounds of order $\gtrsim 1.4$ DN (equivalent to a $\text{DN} = 2.8$ at a gain of 7). Provided the CTE behavior is smooth with respect to time, we can roughly estimate that the CTE loss for the F437N filter was $\lesssim 10\%$ at the time our images were taken.

6.2. ISO/LWS calibration

As explained earlier, the uncertainty quoted on our adopted infrared line fluxes only represents the dispersion in our data sample. Additional uncertainties might come from the calibration itself. According to Swinyard et al. (1998), the uncertainty in the value of the flux for a line is given by the sum (in quadrature) of three terms: one of them

is the dispersion in the measured line flux, and the other two are related to the detectors' responsivity calibration. Although these terms depend on the specific observation considered, typical values are ~ 0.05 and 0.01 . Adding them to the dispersion of our data points, we obtain an overall uncertainty of roughly 13% for either detector. It is possible, however, that this value still underestimates the real uncertainty. Reasons for this are the following:

- 1) Both the drift of the SW2 detector with time and the difference between the SW1 and SW2 detectors are of the order of 10% of the measured flux. This uncertainty is not included in the previous estimation, and should be added to the overall error budget.
- 2) The spectrograph has been calibrated assuming that the source is point-like and centered on the optical axis. Since our object violates at least the first of these assumptions, a correction to the flux should be done. As we stated before, such correction is in principle very small (of order $\sim 1\%$). However, the beam profile of the instrument is not completely understood, being, e.g., much narrower than predicted by optical theory for reasons still unknown (Swinyard et al. 1998; Gry et al. 2001); so we cannot completely exclude that the extension of the source do play a role in our analysis.
- 3) Most density determinations of NGC 6543 are well in excess of our value $N_e = 1650 \text{ cm}^{-3}$; for example, DLW found $N_e[\text{O III}] = 10000 \text{ cm}^{-3}$ and $N_e[\text{O II}] = 4000 \text{ cm}^{-3}$, and Liu et al. (2001) found $N_e[\text{Cl III}] = 4800 \text{ cm}^{-3}$ and $N_e[\text{Ar IV}] = 3900 \text{ cm}^{-3}$ (but, on the other hand, DHEW found $N_e[\text{O III}] = 2000 \text{ cm}^{-3}$). Higher density values would be obtained by increasing the flux of 52μ or decreasing the flux in 88μ , leading in both cases to lower $T_e(\text{O}^{++})_{IR}$.

As an illustrative example of the uncertainties affecting the ISO/LWS data, we repeated the computations adopting the mean 52μ flux of the SW1 detector instead of that of the SW2 detector. This different choice changes $\lambda 5007/52 \mu$ by -0.05 dex and $52 \mu/88 \mu$ by $+0.05$ dex, yielding $T_e = 8100 \text{ K}$ and $N_e = 2000 \text{ cm}^{-3}$.

6.3. Reddening correction

As stated earlier in this paper, we derive a $C(\text{H}\beta)$ value much lower than some of the values found in the literature. However, we see no way of increasing our result. Furthermore, even if this were the case, it would actually imply just a moderate improvement in the $T_e(\text{O}^{++})_{opt}$ result. To illustrate quantitatively this point, we arbitrarily increased $C(\text{H}\beta)$ from 0.07 to 0.30, the largest of the values compiled by Hyung et al. (2001). Given the differential extinction affecting $\lambda 4363$ and $\lambda 5007$, this change translates into a moderate

decrease in the intrinsic $\lambda 5007/\lambda 4363$ ratio, implying an increase of less than 200 K. On the other hand, such increase in $C(\text{H}\beta)$ would enormously affect the $\lambda 5007/52\mu$ ratio, yielding an increase of as much as 1600 K.

7. Summary and conclusions

This work was motivated by the desire to determine self-consistently the physical conditions in the bright core of NGC 6543. We did this by means of two different methods, both based on oxygen line ratios measured across the whole bright halo of the nebula. But, as the work progressed, it became evident that the archival data we used were not optimized for this particular task.

The first method used is the standard nebular-to-auroral temperature diagnostic, and the second is the diagnostic diagram based on infrared lines developed by Dinerstein (1983) and DLW. The N_e and T_e values derived by means of the diagnostic diagram are not compatible with those by DLW, but are in very good agreement to the more recent result by DHEW. On the other hand, the nebular-to-auroral temperature we derive is somewhat lower than the values published in the literature. We discuss some possible causes for these results, related to the accuracy of HST, ISO, and ground-based data.

As a sideproduct of this work, we find that the continuum level differs from the one expected at $T_e \sim T_e(\text{O}^{++})_{opt}$ when $\text{Ly}\alpha$ conversion is neglected. We investigate the possibility that the extra continuum could arise from a high-temperature zone, possibly a shocked region, as suggested by the presence of X rays; however, we could not reproduce the required extra continuum by means of simple plasma models of the X-ray emitting bubble. An alternative explanation we propose is that it is generated by dust scattering of the central star's light. A third possibility, which is the most plausible, is that the additional continuum is enhanced 2-photon emission, originated by conversion of scattered $\text{Ly}\alpha$ photons.

In neither case is it possible to work out a theoretical prescription to compute accurately the continuum intensity that would eliminate the necessity of relying on spectroscopic information. Furthermore, either of these mechanisms would affect equally the slit spectra and the image, so neither would explain the marginally low temperature value that we deduce by means of the HST data. As a result, the most important source of uncertainty in the determination of the optical temperature is the continuum subtraction in the $\lambda 4363$ image; a specific conclusion we draw is that it is not possible with these data to obtain an accurate bidimensional temperature map of the nebula. More generally, we review several possible causes of error that could be introducing a bias in our work. The calibration uncertainty of

WFPC2 at very low DNs introduces perhaps an additional uncertainty. The HST fluxes at other wavebands and the ISO data are probably more robust, but the overall uncertainty could still be somewhat higher than 10%. In the case of HST data, a fraction of this uncertainty might arise from the contribution of different lines to the observed fluxes; in the case of ISO data, the overall accuracy is probably of order $\sim 13\%$.

Although NGC 6543 has been previously studied by many authors, most measurements have been made with small apertures which sample only a small fraction of the nebula. One disadvantage of this approach is that it limits the possibility to compare among different results. On the contrary, the data we use sample the whole region, allowing us to do a self-consistent analysis which eliminates the need of assumptions about the ionization structure. Furthermore, the use of lines of the same ion allows a self-consistent determination of N_e and T_e , independent of assumptions on the ionization structure. Unfortunately, the available archival data were not specifically designed for this analysis, and contain sources of uncertainties that are, in many cases, quite difficult to estimate. We think therefore that our results on the physical conditions in NGC 6543 are somewhat biased, and we definitely exclude the possibility of using these data to derive sensible temperature maps unless specifically designed data are obtained that provide a safe way of measuring the continuum and line contribution inside each filter. Our results are, however, largely informative for what concerns delicate technical issues that must be taken into account when studies of this kind are carried out. In particular, we draw the attention, throughout this paper, to complex aspects of the use of data from large archives, in the hope that the authors of future similar works will be motivated to provide an explicit description of the crucial assumptions underlying their analyses.

We thank Jesús Maíz-Apellániz for helping us through the jungle of WFPC2 data. We are also very grateful to Grażyna Stasińska for an early reading of this paper and several useful suggestions, and Robert O’Dell and Antonio Mampaso for insightful comments. It is also a pleasure to acknowledge Chris Lloyd and the ISO helpdesk for their keen answers to our questions. Support from the HST helpdesk is also acknowledged. We thank Luis Cuesta, David Axon and Andrew Robinson, who contributed to obtain the ground based spectroscopic data. Two anonymous referees provided us with several useful suggestions and criticism, which were essential to improve the paper. VL is supported by a Marie Curie Fellowship of the European Community programme “*Improving Human Research Potential and the Socio-economic Knowledge Base*” under contract number HPMF-CT-2000-00949. This work has been partially financed by DGICYT grants PB98-0521 and AYA-2001-3939-C03-01. This research has made use of NASA’s Astrophysics Data System Bibliographic Services, and it is really difficult to figure out how it was possible to work before the ADS

era. This work is based on observations made with the NASA/ESA Hubble Space Telescope, obtained from the data archive at the Space Telescope Science Institute. STScI is operated by the association of Universities for Research in Astronomy, Inc. under the NASA contract NAS 5-26555. The Isaac Newton Telescope is operated on the island of La Palma by the Isaac Newton Group of Telescopes in the Spanish Observatorio del Roque de Los Muchachos of the Instituto de Astrofísica de Canarias.

REFERENCES

- Baggett, S., & McMaster, M. (editors) 2002, WFPC2 Data Handbook, version 4.0 (Baltimore: STScI)
- Balick, B., Wilson, J., & Hajian, A. R. 2001, *AJ*, 121, 354
- Biretta, J. et al. 2001, WFPC2 Instrument Handbook, Version 6.0, (Baltimore: STScI)
- Bohuski, T. J., Dufour, R. J., & Osterbrock, D. E. 1974, *ApJ*, 188, 529
- Brown, R. L., & Mathews, W. G. 1970, *ApJ*, 160, 939
- Cardelli, J. A., Clayton, G. C., & Mathis, J. S. 1989, *ApJ*, 345, 245
- Chu, Y., Guerrero, M. A., Gruendl, R. A., Williams, R. M., & Kaler, J. B. 2001, *ApJ*, 553, L69
- Dinerstein, H. L. 1983, *IAU Symp. 103: Planetary Nebulae*, 103, 79
- Dinerstein, H. L., Haas, M. R., Erickson, E. F., & Werner, M. W. 1995, *ASP Conf. Ser. 73: From Gas to Stars to Dust*, 387
- Dinerstein, H. L., Lester, D.F., & Werner, M. W. 1985, *ApJ*, 291, 561
- Ferland, G. J. 1996, *Hazy, a Brief Introduction to Cloudy*, University of Kentucky Department of Physics and Astronomy Internal report
- Gry, C., et al. 2001, *The ISO Handbook*, vol. IV, LWS - The Long Wavelength Spectrometer, version 1.2
- Hyung, S., Aller, L. H., Feibelman, W. A., Lee, W. B., & de Koter, A. 2000, *MNRAS*, 318, 77
- Hyung, S., Mellema, G., Lee, S.-J., and Kim, H. 2001, *A&A*, 378, 587

- Kaler, J. B. 1983, *ApJ*, 264, 594
- Kaler, J. B., Shaw, R. A., & Browning, L. 1997, *PASP*, 109, 289
- Kingsburgh, R. L., López, J. A., & Peimbert, M. 1996, *ASP Conf. Ser.* 99: Cosmic Abundances, 350.
- Lame, N. J., Harrington, J. P., & Borkowski, K. 1997, *IAU Symp.* 180: Planetary Nebulae, 180, 252
- Liu, X.-W., Barlow, M. J., Cohen, M., et al. 2001, *MNRAS*, 323, 343
- Middlemass, D., Clegg, R. E. S., & Walsh, J. R. 1989, *MNRAS*, 239, 1
- Miranda, L. F. & Solf, J. 1992, *A&A*, 260, 397
- O'Dell, C. R. & Doi, T. 1999, *PASP*, 111, 1316
- O'Dell, C. R., Peimbert, M., and Peimbert, A. 2003, *AJ* (submitted)
- Osterbrock, D. E. 1989, *Astrophysics of Gaseous Nebulae and Active Galactic Nuclei* (University Science Books, California)
- Peimbert, M. 1967, *ApJ*, 150, 825
- Peimbert, M. 1995, *The Analysis of Emission Lines: A Meeting in Honor of the 70th Birthdays of D. E. Osterbrock & M. J. Seaton*, proceedings of the Space Telescope Science Institute Symposium, 1994, Eds.: Robert Williams and Mario Livio, Cambridge University Press, p.165
- Peimbert, M., Torres-Peimbert, S., & Luridiana, V. 1995, *Revista Mexicana de Astronomía y Astrofísica*, 31, 131
- Persi, P., Cesarsky, D., Marenzi, A. R., Preite-Martinez, A., Rouan, D., Siebenmorgen, R., Lacombe, F., & Tiphene, D. 1999, *A&A*, 351, 201
- Reed, D. S., Balick, B., Hajian, A. R., Klayton, T. L., Giovanardi, S., Casertano, S., Panagia, N., & Terzian, Y. 1999, *AJ*, 118, 2430
- Rubin, R.H., et al. 2002, *MNRAS*, in press
- Storey, P. J. & Hummer, D. G. 1995, *MNRAS*, 272, 41
- Swinyard, B. M. et al. 1998, *Proc. SPIE*, 3354, 888

Whitmore, B., Heyer, I., & Casertano, S. 1999, PASP, 111, 1559

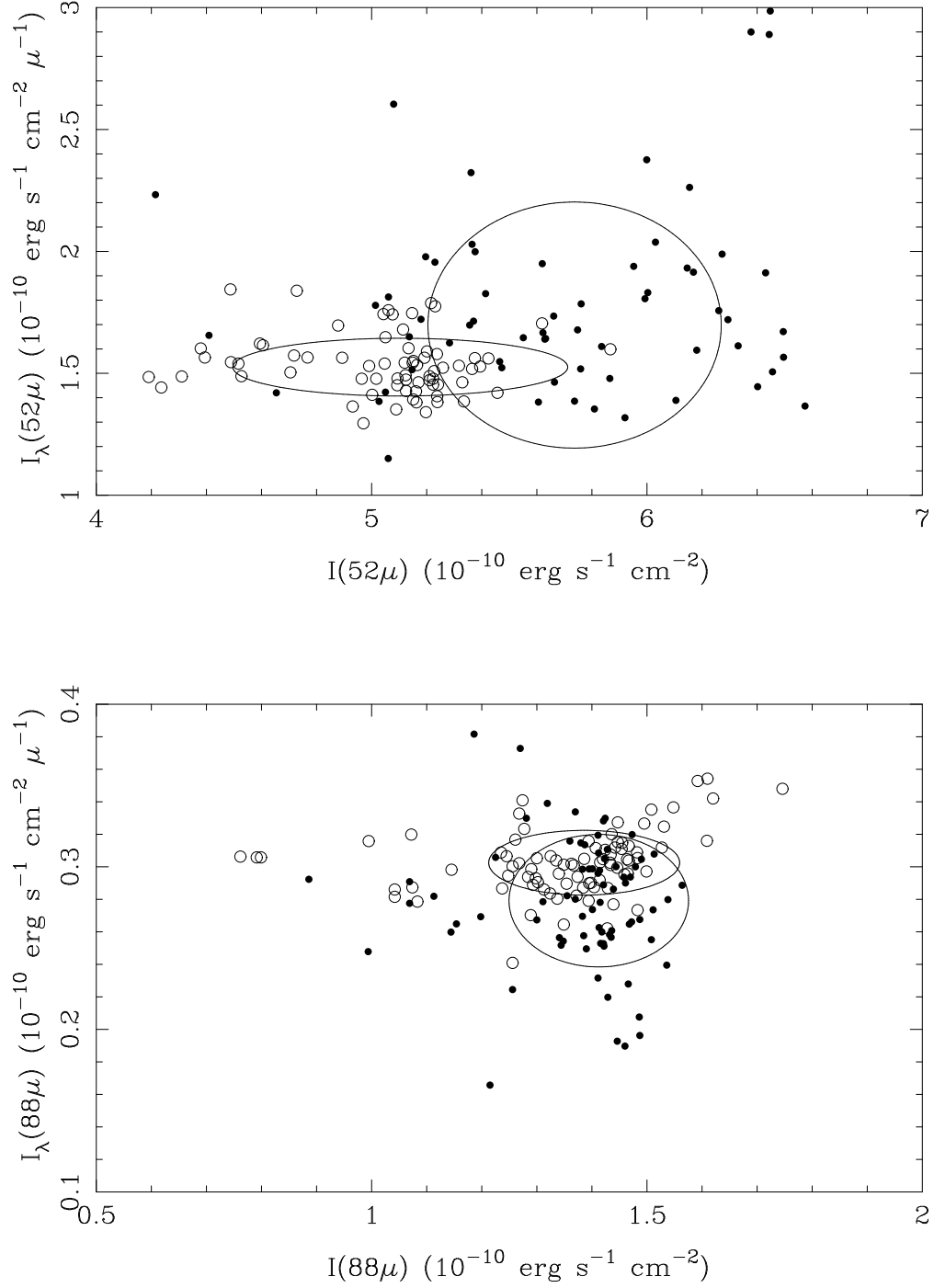


Fig. 1.— ISO 52μ and 88μ line vs. continuum intensities for our sample, with the 1-σ ellipses overplotted. Upper panel: dots are SW1 data, open circles SW2 data. Lower panel: dots are SW5 data, open circles LW1 data.

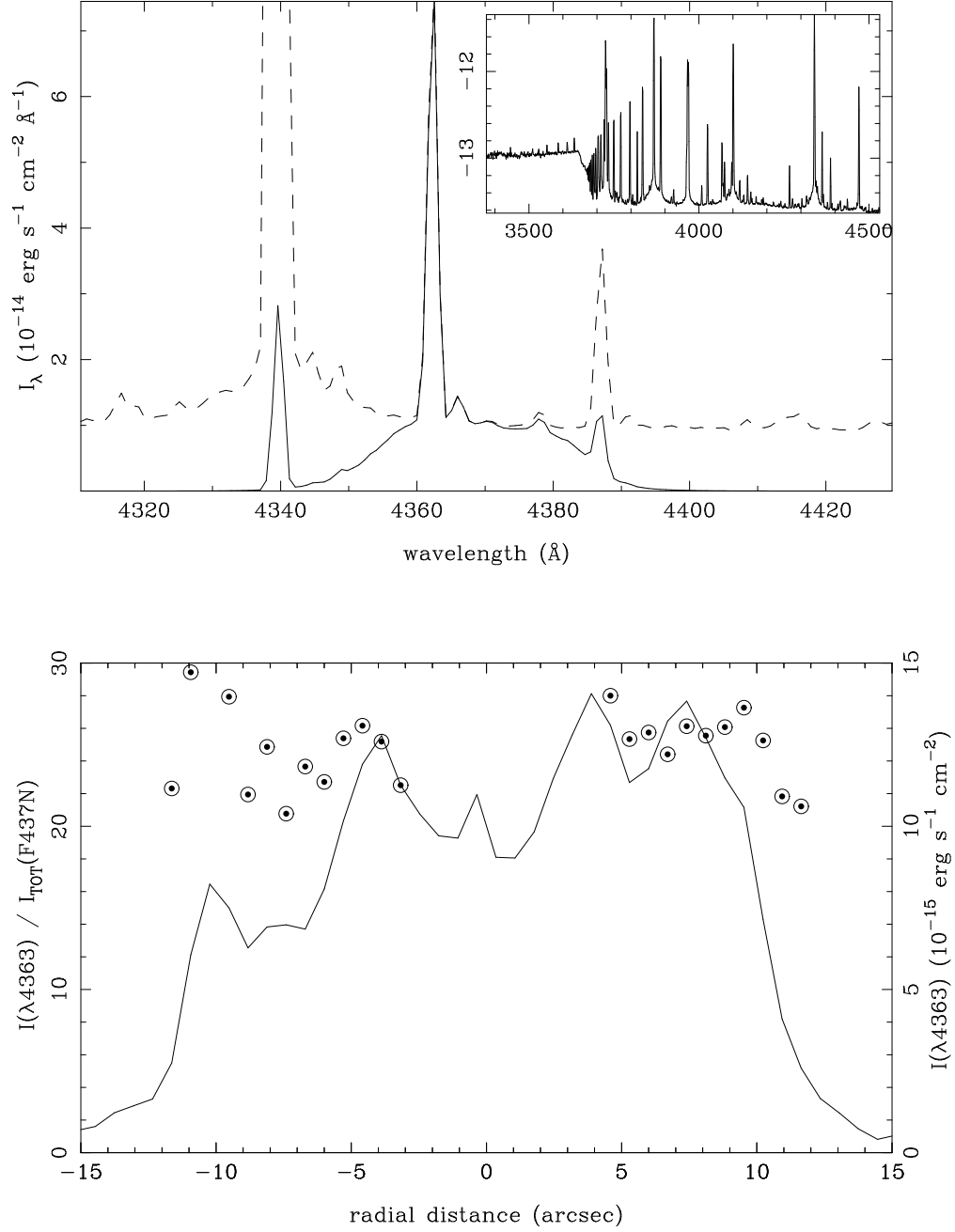


Fig. 2.— (top) Nebular spectrum of NGC 6543 along position angle 5° in the wavelength region around λ 4363. The dashed line is the actual spectrum; the full line is the spectrum convolved with the F437N filter response (the total system peak response of 0.03 has been divided out). The inset shows a sample of the spectrum along the slit in a logarithmic scale. (bottom) The dotted circles (left handside scale) show the percent of the total intensity of radiation through the HST filter F437N that is contributed by the λ 4363 line intensity. Also plotted is the variation of the λ 4363 intensity along the slit (full line, right hand side scale).

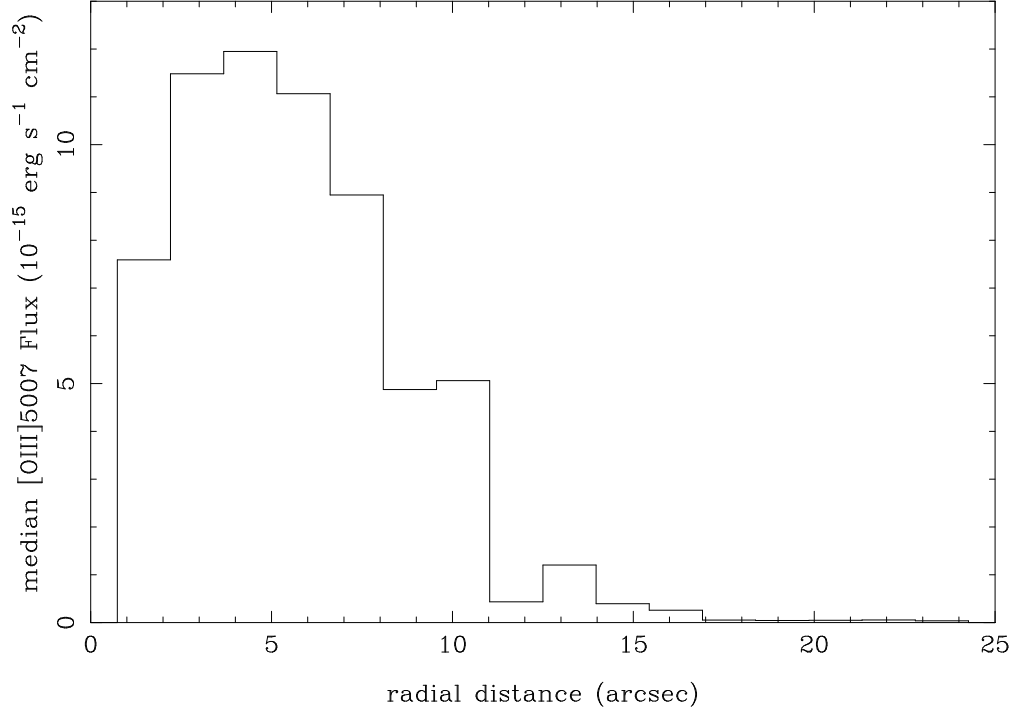


Fig. 3.— Median value of [O III] λ 5007 on the HST image.

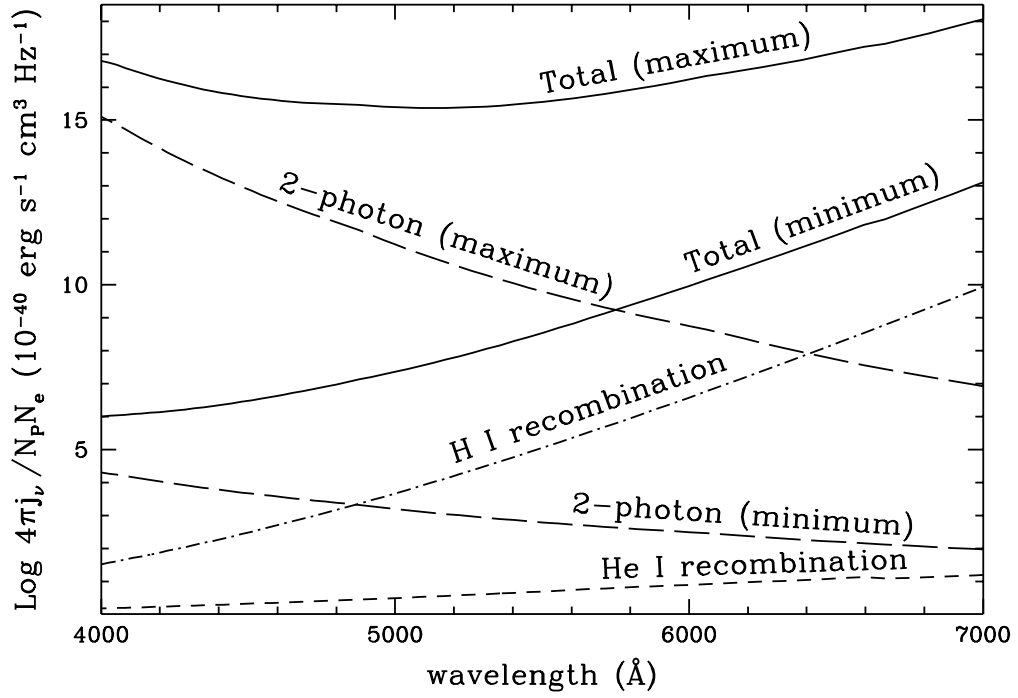


Fig. 4.— Hydrogen and helium continua at $T_e = 8000$ K.

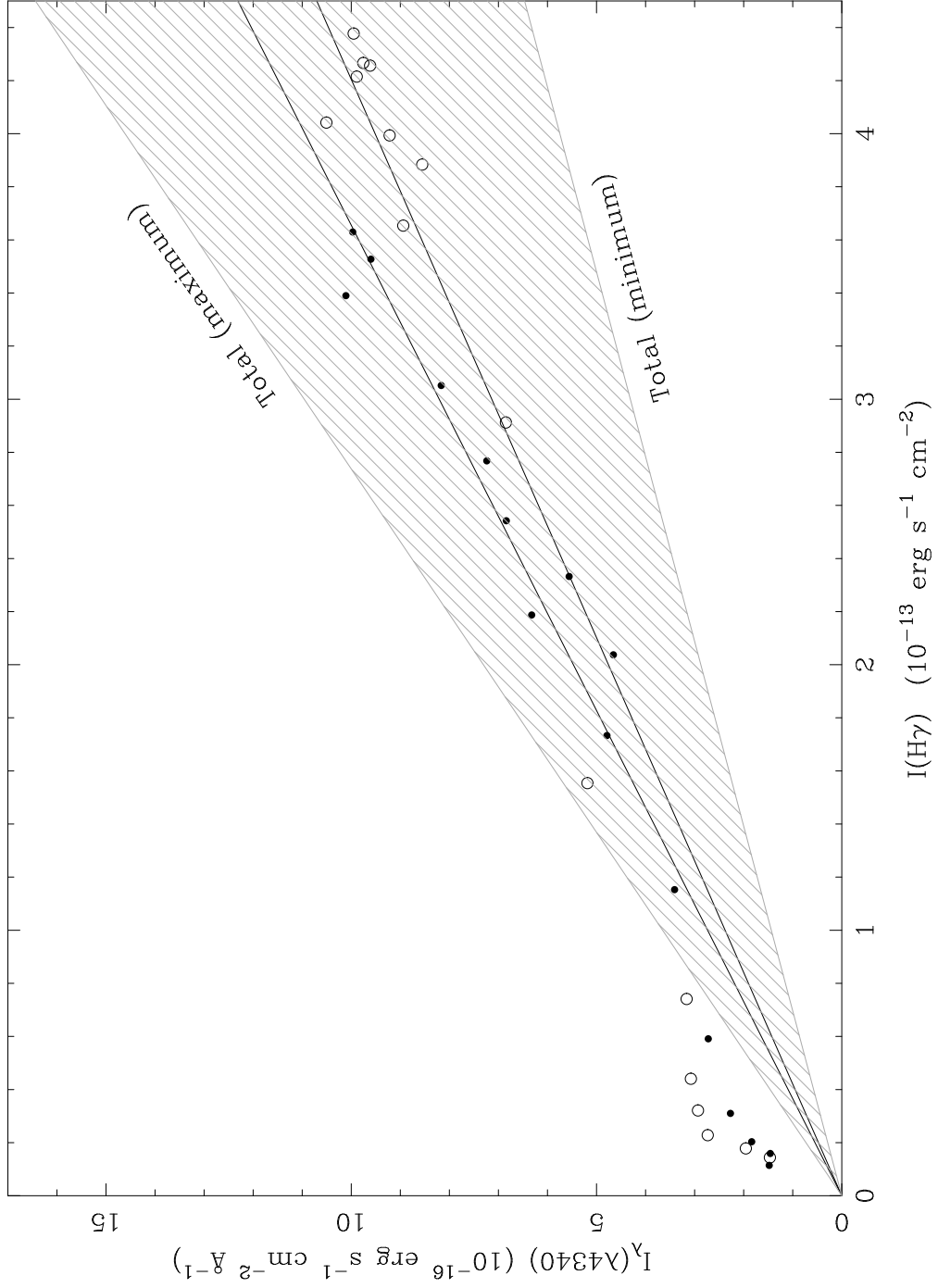


Fig. 5.— Observed $\text{H}\gamma$ and nearby continuum fluxes measured along the INT slit, as a function of the distance from the central star. The shaded region corresponds to the region predicted by recombination theory. Dots and open circles represent the two directions along the slit, and the two solid lines the corresponding best-fit linear relations.

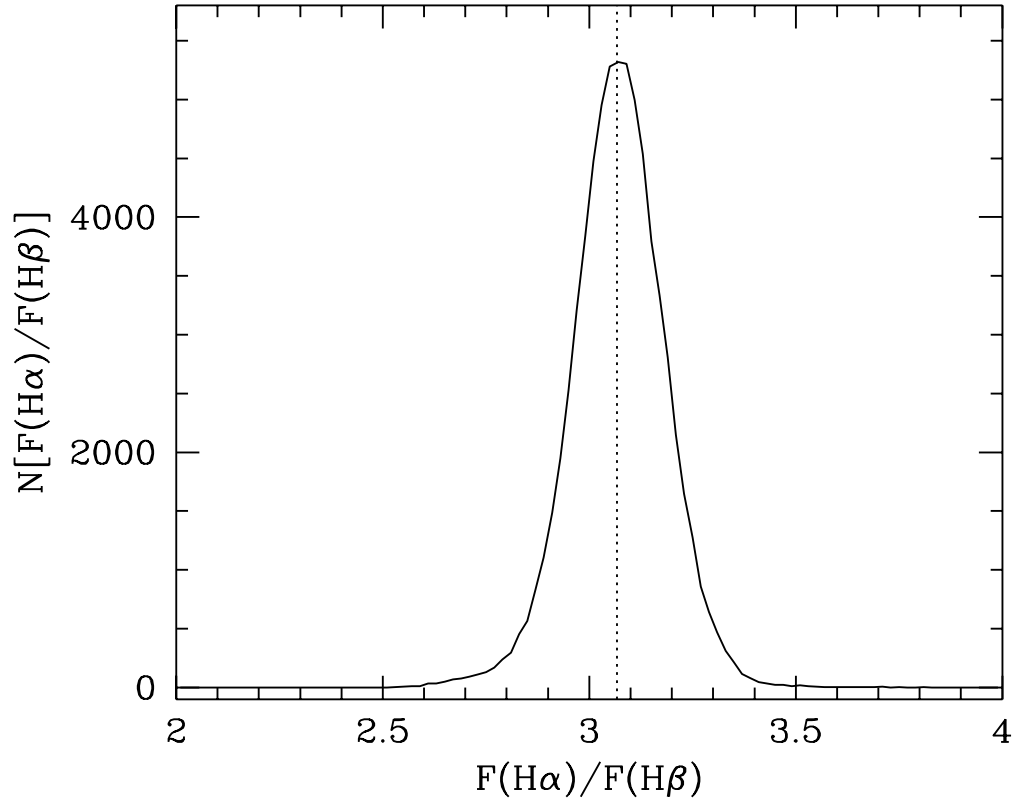


Fig. 6.— Pixel-by-pixel $F(\text{H}\alpha)/F(\text{H}\beta)$ histogram.

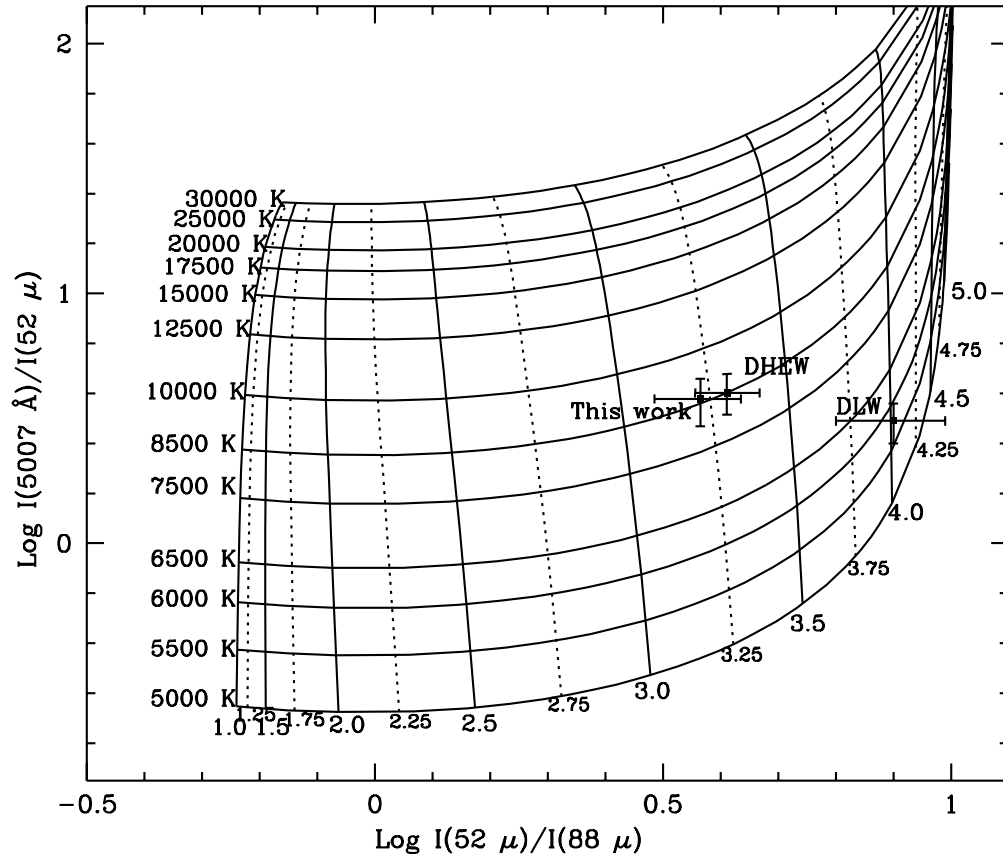


Fig. 7.— [O III] infrared-line diagnostic diagram.

Table 1. ISO LWS archive spectra.

| Epoch | Date | TDT | Proposal ID |
|----------|-------------|----------|-------------|
| Epoch I | 05-Jun-1996 | 20101905 | CAL_R196 |
| | 07-Jun-1996 | 20301905 | CAL_R203 |
| | 14-Jun-1996 | 21003105 | CAL_R210 |
| | 21-Jun-1996 | 21704705 | CAL_R217 |
| | 27-Jun-1996 | 22301705 | LWS_R223 |
| | 04-Jul-1996 | 23001905 | CAL_R230 |
| | 11-Jul-1996 | 23705405 | CAL_R237 |
| | 18-Jul-1996 | 24404805 | CAL_R244 |
| | 24-Jul-1996 | 25100805 | CAL_R251 |
| | 28-Jul-1996 | 25500701 | DUST4_A |
| | 31-Jul-1996 | 25800905 | CAL_R258 |
| Epoch II | 02-Dec-1997 | 74801614 | CAL_R748 |
| | 09-Dec-1997 | 75500604 | CAL_R755 |
| | 16-Dec-1997 | 76201203 | CAL_R762 |
| | 23-Dec-1997 | 76902404 | CAL_R769 |
| | 30-Dec-1997 | 77602002 | CAL_R776 |
| | 06-Jan-1998 | 78300202 | CAL_R783 |
| | 13-Jan-1998 | 79000702 | CAL_R790 |
| | 20-Jan-1998 | 79700402 | CAL_R797 |
| | 27-Jan-1998 | 80401402 | CAL_R804 |

Table 2. ISO/LWS fluxes.

| Line | Detector | Epoch ^c | Line intensity ^a | | Continuum flux ^b | |
|----------|----------|--------------------|-----------------------------|----------|-----------------------------|----------|
| | | | Median | σ | Median | σ |
| 52 μ | SW1 | I | 5.58 | 0.50 | 1.66 | 0.29 |
| | | II | 6.10 | 0.43 | 1.91 | 0.68 |
| | | I+II | 5.74 | 0.53 | 1.70 | 0.50 |
| | SW2 | I | 5.06 | 0.66 | 1.54 | 0.11 |
| | | II | 5.15 | 0.52 | 1.49 | 0.12 |
| | | I+II | 5.10 | 0.61 | 1.53 | 0.12 |
| 88 μ | SW5 | I | 1.40 | 0.18 | 2.69 | 0.47 |
| | | II | 1.42 | 0.13 | 2.89 | 0.29 |
| | | I+II | 1.41 | 0.16 | 2.79 | 0.41 |
| | LW1 | I | 1.34 | 0.14 | 2.92 | 0.19 |
| | | II | 1.44 | 0.20 | 3.09 | 0.17 |
| | | I+II | 1.39 | 0.17 | 3.02 | 0.20 |

^aIn units 10^{-10} erg sec⁻¹ cm⁻².

^bIn units 10^{-10} erg sec⁻¹ cm⁻² μ^{-1} for SW1 and SW2, and 10^{-11} erg sec⁻¹ cm⁻² μ^{-1} for SW5 and LW1.

^cSee text and Table 1

Table 3. HST archive images.

| Line ^a | Filter | Dataset | Exposure (s) | PHOTFLAM (erg s ⁻¹ cm ⁻² Å ⁻¹) | RECTW (Å) |
|-------------------|--------|-----------|-----------------|---|--------------|
| [O III] λ 4363 | F437N | U27Q0103T | 1200 | 7.400×10^{-16} | 31.829 |
| | | U27Q0104T | 1200 | | |
| Hβ | F487N | U27Q0105T | 500 | 3.945×10^{-16} | 33.921 |
| | | U27Q0106T | 900 | | |
| [O III] λ 5007 | F502N | U27Q0107T | 200 | 3.005×10^{-16} | 35.781 |
| | | U27Q0108T | 600 | | |
| | | U27Q0109T | 200 | | |
| | | U27Q010AT | 600 | | |
| Hα | F656N | U27Q010FT | 200 | 1.461×10^{-16} | 28.336 |
| | | U27Q010GT | 600 | | |
| [N II] λ 6584 | F658N | U27Q010HT | 500 | 1.060×10^{-16} | 39.232 |
| | | U27Q010IT | 500 | | |

^aMost important emission line included in the passband.

Table 4. Frequency dependence of some continuum-emission coefficients (in 10^{-40} erg $\text{sec}^{-1} \text{ cm}^3 \text{ Hz}^{-1}$) at $T_e = 8000$ K.

| | λ 4363 | λ 5007 | λ 6563 |
|--|----------------|----------------|----------------|
| H I ^a | 2.196 | 3.687 | 8.431 |
| He I ^a | 2.544 | 4.502 | 10.12 |
| 2-photon continuum, minimum ^b | 3.827 | 3.193 | 2.175 |
| 2-photon continuum, maximum ^c | 13.429 | 11.204 | 7.632 |

^aIncluding recombination and bremsstrahlung.

^bNeglecting Ly α -to-2-photon conversion.

^cIncluding maximal Ly α -to-2-photon conversion.

Table 5. Summary of fluxes and diagnostics.

| | DLW | | This work | |
|------------------------------------|------------------------|-----------------|------------------------|-----------------|
| | $F(\lambda)$ | $I(\lambda)$ | $F(\lambda)$ | $I(\lambda)$ |
| $\lambda 5007^a$ | 1.65 ± 0.25^b | 2.70 ± 0.40 | 1.65^c | 1.93 ± 0.29 |
| $\lambda 4363^d$ | ... | ... | 3.28 ± 0.40 | 3.95 ± 0.84 |
| $52\mu^a$ | | 8.79 ± 0.97 | | 5.10 ± 0.61 |
| $88\mu^a$ | | 1.10 ± 0.20 | | 1.39 ± 0.17 |
| $\log \lambda 5007 / \lambda 4363$ | 2.56 | | 2.69 ± 0.10 | |
| $\log \lambda 5007 / 52\mu$ | $0.49^{+0.07}_{-0.09}$ | | $0.58^{+0.07}_{-0.09}$ | |
| $\log 52\mu / 88\mu$ | $0.90^{+0.09}_{-0.10}$ | | $0.56^{+0.07}_{-0.08}$ | |
| $T_e(\text{O}^{++})_{opt}$ | 7900 | | 7500 ± 450 | |
| $T_e(\text{O}^{++})_{IR}$ | 5800 ± 300 | | 8600 ± 500 | |
| $\log N_e(\text{O}^{++})_{IR}$ | $4.0^{+\infty}_{-0.4}$ | | 3.22 ± 0.12 | |

^aIn units of $10^{-9} \text{ erg s}^{-1} \text{ cm}^{-2}$.

^bComputed by us with the $C(\text{H}\beta)$ quoted by DLW.

^cNo uncertainty have been quoted on $F(\lambda 5007)$, since our estimated uncertainty on $F(\lambda 5007)$ includes only the uncertainty on the reddening correction (Section 5).

^dIn units of $10^{-12} \text{ erg s}^{-1} \text{ cm}^{-2}$.